npj Computational Materials

www.nature.com/npjcompumats

ARTICLE OPEN

Check for updates

Chiral logic computing with twisted antiferromagnetic magnon modes

Chenglong Jia[1]✉, Min Chen[1], Alexander F. Schäffer[2] and Jamal Berakdar[2]✉

Antiferromagnetic (AFM) materials offer an exciting platform for ultrafast information handling with low cross-talks and compatibility with existing technology. Particularly interesting for low-energy cost computing is the spin wave-based realization of logic gates, which has been demonstrated experimentally for ferromagnetic waveguides. Here, we predict chiral magnonic eigenmodes with a finite intrinsic, magnonic orbital angular momentum ℓ in AFM waveguides. ℓ is an unbounded integer determined by the spatial topology of the mode. We show how these chiral modes can serve for multiplex AFM magnonic computing by demonstrating the operation of several symmetry- and topology-protected logic gates. A Dzyaloshinskii–Moriya interaction may arise at the waveguide boundaries, allowing coupling to external electric fields and resulting in a Faraday effect. The uncovered aspects highlight the potential of AFM spintronics for swift data communication and handling with high fidelity and at a low-energy cost.

npj Computational Materials (2021)7:101 ; https://doi.org/10.1038/s41524-021-00570-0

INTRODUCTION

Magnetic materials are essential elements in data storage, information processing, and sensory devices. Their low-energy excitations, the spin waves with magnons as quanta of excitations, can be utilized to transmit and process information at low-energy cost and without heat dissipation due to Ohmic losses[1–3]. Recent research on AFM[4–11] demonstrated their potential for the next generation of spintronics and optoelectronic devices. Experiments evidenced that the AFM ordering is switchable on THz time scale by charge current or THz pulses. Material-wise, AFM structures are well compatible with a variety of material classes and amenable to nanopatterning. For instance, synthetic AFM samples (SyAF) were fabricated out of two magnetic layers that are coupled antiferromagnetically[12–14]. SyAFs allow thus creating AFM/FM heterostructures. The field is further fuelled by the uncovered properties of van der Waals coupled 2D materials[15–19], which may be viewed (depending on their synthesis) as a type of FM, AFM or SyAF structure. Notably, ref. [20] demonstrated the excitation and the long-distance AFM magnon transport in the quasi-2D van der Waals AFM $MnPS_3$.

Generally, magnons in AFM[21,22] are qualitatively different from their FM counterpart: (1) FM magnons are always right-handed. In contrast, AFM have two degenerate spin wave eigenmodes of opposite chirality, referred to as right- and left-handed magnons depending on the precessional handedness of the AFM order parameter (the Néel vector, cf. Fig. 1). Combining these two polarizations, any polarization state can be produced, offering a way to encode information based on polarization-states. (2) AFM materials do not suffer from cross talks, as demagnetizing fields are minor, and hence signals carried by AFM excitation are robust to external magnetic perturbations. The small intrinsic magnetization which emerges upon a spatiotemporal variation of the AFM order parameter may be utilized to act on the dynamics of magnetic textures and spin currents. (3) Being much fast than FM magnons, AFM spin waves can be employed for swift data transfer.

Another feature of AFM magnons is demonstrated in this work: AFM waveguides support chiral magnonic eigenmodes that carry a well-defined amount ℓ of magnonic orbital angular momentum (OAM) (with respect to the propagation direction). ℓ is unbounded and associated with the spatial topology or the "twist" of the eigenmode extending over the whole waveguide. We demonstrate how the twisted modes serve for realizing a class of symmetry-protected logic gates and for multiplex data transfer[23–26]. The operation of the gates is robust, for the twisted beams are found as eigenmodes of the waveguide with a dispersion allowing for forming signals as fast as AFM magnonics. Waveguide boundaries can host a Dzyaloshinskii–Moriya[27,28] interaction (DMI) due to the break of inversion symmetry. We find DMI is useful for triggering and steering twisted modes. The analytic predictions are ubiquitous, meaning that twisted AFM magnons should appear in conventional AFM, SyAF, or van-der-Waals-AF cylindrical waveguides. We present a general theory and demonstrate with full-numerical simulations the character and the functionalization of twisted modes for a prototypical NiO AFM waveguide for a demonstration.

RESULTS AND DISCUSSION

Chiral antiferromagnetic magnons

As a magnonic waveguide we consider a cylindrical wire made of a G-type AFM[29] with an axis aligned along with the AFM easy ($\mathbf{e}_z$) direction (cf. Fig. 1). In practice, the waveguide can be deposited or imprinted on a substrate or be part of integrated magnonic circuits. For capturing the low-energy AFM dynamics, it is adequate to start from the Heisenberg Hamiltonian

$$\mathcal{H} = \frac{J}{2}\sum_{ij}\mathbf{S}_i\cdot\mathbf{S}_j - \frac{K_z}{2}\sum_i(\mathbf{S}_i\cdot\mathbf{e}_z)^2, \tag{1}$$

where $J>0$ stands for the strength of the (uniform) AFM exchange coupling between neighboring spins $\mathbf{S}_i$ localized at lattice sites i with a lattice distance a. The uniaxial anisotropy energy

[1]Key Laboratory for Magnetism and Magnetic Materials of the Ministry of Education & Lanzhou Center for Theoretical Physics, Lanzhou University, Lanzhou, China. [2]Institut für Physik, Martin-Luther-Universität Halle-Wittenberg, Halle (Saale), Germany. ✉email: cljia@lzu.edu.cn; jamal.berakdar@physik.uni-halle.de

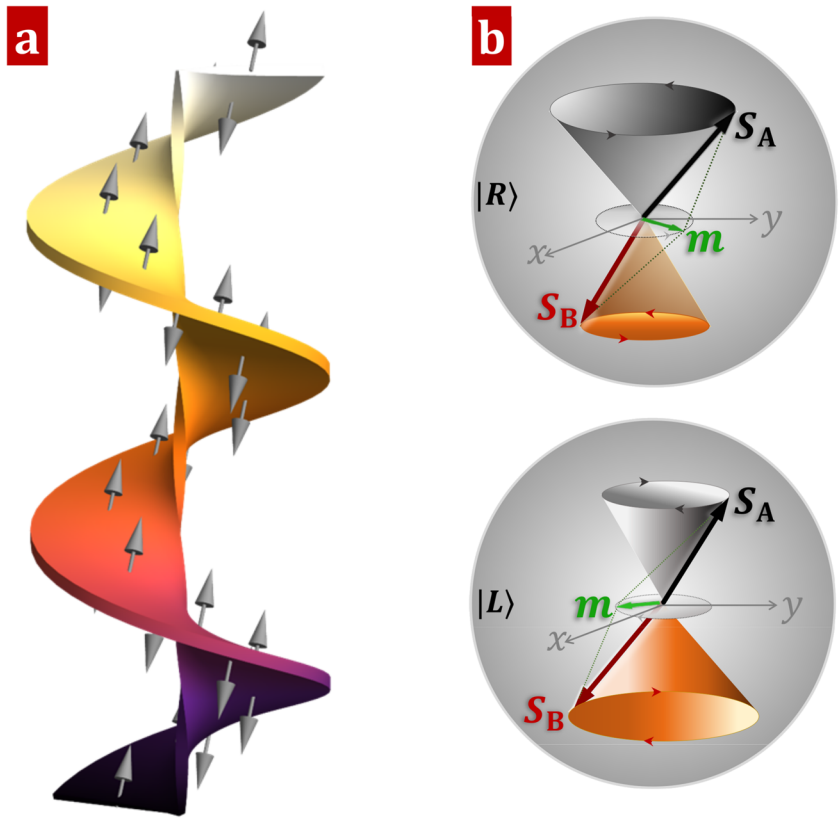

Fig. 1 Schematic representation of twisted magnon beams in AFM waveguide. a Twisted magnon beams propagating along a cylindrical AFM waveguide with two magnetic sublattices A (up arrows) and B (down arrows). **b** Degenerate right- and left-handed spin wave modes, $|L\rangle$ and $|R\rangle$ dominated by the sublattice A and B, respectively. The small magnetization (green arrows) is defined as $\mathbf{m} = (\mathbf{S}_A + \mathbf{S}_B)/2S$).

contribution (with strength $\propto K_z > 0$) is large enough to suppress quantum fluctuations enforcing so a collinear (Néel) ground state aligned with the easy axis (cf. Fig. 1). The spin dynamics follows Heisenberg's equation of motion $d\mathbf{S}_i/dt = -i/\hbar[\mathbf{S}_i, \mathcal{H}] = \mathbf{S}_i \times (K_z \mathbf{S}_i^z - \sum_{j\in i} J\mathbf{S}_j)$. Low-energy excitations, meaning AFM spin waves are described[21] by introducing the classical dimensionless unit vector field $\mathbf{s}_i = \mathbf{S}_i/S$, where $|\mathbf{S}_i| = S$ for all sites. The spin waves are then transversal excitations propagating according to

$$i\hbar \frac{ds_i^-}{dt} = -\left(K_S s_i^z - \sum_{j\in i} J_S s_j^z\right) s_i^- - s_i^z \sum_{j\in i} J_S s_j^-, \tag{2}$$

with $s_i^\pm := s_i^x \pm i s_i^y$. $K_S = K_z S\hbar$, $J_S = JS\hbar$ are respectively the anisotropy and exchange energies. Using a plane-wave ansatz $s_i^-(t) \sim e^{i(\mathbf{k}\cdot\mathbf{r}_i - \omega_k t)}$, one infers the dispersion relation for spin waves as $E_k^2 = \hbar^2\omega_k^2 = (K_S + \zeta J_S)^2 - (\zeta J_S \gamma_k)^2$ where ζ is the coordination number ($\zeta = 2, 4, 6$ for respectively one-dimensional spin chain, two-dimensional square lattice, and a three-dimensional cubic lattice). $\gamma_k = \sum_{j\in i} e^{i\mathbf{k}\cdot\mathbf{r}_{ji}}/\zeta$. The same dispersion follows from a Holstein–Primakoff approach[30,31].

AFM magnonic Dirac dynamics

The physics of AFM low-energy excitations is most transparent upon a mapping onto two sub-lattices[32–36] denoted A and B with antiparallel spins (cf. Fig. 1a). The ordering in each sublattice is FM but a translation by a lattice vector transforms $\mathbf{S}(\mathbf{r} + \mathbf{a}) \to -\mathbf{S}(\mathbf{r})$, meaning that the translational invariance is broken. Thus, the AFM Heisenberg system is mappable onto an antiferromagnetic (AFM) CP^1 model[36]. Note, the AFM Hamiltonian is still invariant under the combined time-reversal ($\mathcal{T}$) and sub-lattice exchange ($\mathcal{I}$), a fact underlying the degeneracy of the two chiral magnon modes. Equation (1) is, in addition, invariant under global spin rotation around the z-axis, and thus the z-component of the total spin is a good quantum number. For a further insight, let us follow Haldane[32] (see also[33,35,36]) and consider small sublattice-dependent fluctuations around the one-dimensional Néel ground state[32]. To do so, one introduces $\mathbf{s}_i^A = (\mathbf{a}_i + \sqrt{1 - \mathbf{a}_i^2}\,\mathbf{e}_z)$ and $\mathbf{s}_i^B = (\mathbf{b}_i - \sqrt{1 - \mathbf{b}_i^2}\,\mathbf{e}_z)$, where $|\mathbf{a}_i| \ll 1$ and $|\mathbf{b}_i| \ll 1$. Linearizing Eq. (2) and noting that $\mathbf{a}_j = \mathbf{a}_i + (\mathbf{r}_{ij}\cdot\nabla)\mathbf{a}_i + \frac{1}{2}\mathbf{r}_{ij}^2\nabla^2\mathbf{a}_i + \ldots$ (and proceeding similarly for $\mathbf{b}_i$), we arrive at the continuum Hamiltonian (valid up to the second-order derivatives)

$$i\hbar \frac{d\psi_i^+}{dt} = \mathcal{H}_D \psi_i^+, \tag{3}$$

where $\psi_i^+(z,t) = (a_i^+, b_i^+)^T$ is the two-component Dirac spinor, and ($\tilde{\partial}_z := 2a\,\partial/\partial z$)

$$\mathcal{H}_D = \begin{bmatrix} K_S + 2J_S & 2J_S - J_S\tilde{\partial}_z + J_S\tilde{\partial}_z^2/2 \\ -2J_S - J_S\tilde{\partial}_z - J_S\tilde{\partial}_z^2/2 & -K_S - 2J_S \end{bmatrix}. \tag{4}$$

The first-order derivative ($\sim J_S\tilde{\partial}_z$) in $\mathcal{H}_D$ is a parity-breaking term and as such is not invariant under sublattice exchange ($A \leftrightarrow B$) in the G-type AFMs. This term introduces a finite precessional phase difference between the sublattice A and B. In the long-wavelength limit of plane-wave ansatz, the eigenenergies of the Dirac Hamiltonian Eq. (3) are $E_k = \pm\left[J_S^2 k_z^2 + K_S(K_S + 4J_S)\right]^{1/2}$ with the corresponding eigenmodes

$$\psi_L^+ = \begin{bmatrix} \cosh\frac{\vartheta}{2} \\ -e^{i\varphi}\sinh\frac{\vartheta}{2} \end{bmatrix} \text{ and } \psi_R^+ = \begin{bmatrix} -\sinh\frac{\vartheta}{2} \\ e^{i\varphi}\cosh\frac{\vartheta}{2} \end{bmatrix}, \tag{5}$$

where $\cosh\vartheta = (K_S + 2J_S)/|E_k|$ and $\tan\varphi = J_S k_z/(2J_S - J_S k_z^2/2)$[37].

ψ_L^+ (ψ_R^+) with eigenfrequency $\omega_k > 0$ ($\omega_k < 0$) describes the left-circularly (right-circularly) polarized modes dominated by the precession in A (B) sublattice, as illustrated in Fig. 1b. The opposite holds true for the complex conjugate $\psi_i^- = (a_i^-, b_i^-)^T$. In the following, we take the positive eigenfrequency modes, $|L\rangle \equiv \psi_L^+$ and $|R\rangle \equiv \psi_R^-$ as the chirally complete basis for AFM magnons. Although $\mathcal{H}_D$ is not Hermitian, the chiral basis can be easily normalized by applying a momentum-dependent factor, such that $\langle L|L\rangle/\mathcal{N}_k = \langle R|R\rangle/\mathcal{N}_k = 1$ with $\mathcal{N}_k = \cosh\vartheta$ and the averaged $\langle L|R\rangle_k = -\langle \sinh\vartheta\rangle_k \equiv 0$. Considering the spin precession around the z-axis, we define a chirality (chiral charge) as $C_L = \langle L|\sigma_z|L\rangle = 1$ and $C_R = \langle R|\sigma_z|R\rangle = -1$, clearly, $|L\rangle$ and $|R\rangle$ have particle-hole symmetry. Note, the AFM magnon chirality is intrinsic and independent of the propagation direction of magnons. Its origin stem from the symmetry of the AFM system. Hence, it is useful to employ the magnon chirality for a non-volatile encoding of information, as explicitly demonstrated below.

Magnonic Klein–Gordon dynamics

When applying Haldane's mapping procedure, no apparent parity-breaking exchange term appears in the continuum energy function. The parity-breaking term is important to correctly capture the intrinsic magnetization, as evident in the continuum limit of the free energy of AFM magnons. Let us employ the staggered field[35] $\mathbf{n} = (\mathbf{S}_A - \mathbf{S}_B)/(2S)$ and the intrinsic magnetization $\mathbf{m} = (\mathbf{S}_A + \mathbf{S}_B)/(2S)$. For large and isotropic AFM exchange $J \gg K_z$, the total Lagrangian density reads[32,33,35],

$$\mathcal{L} = \rho_s \mathbf{m}\cdot(\partial_t \mathbf{n}\times\mathbf{n}) - \frac{\mathbf{m}^2}{2\chi_m} - \frac{A}{2}(\partial_\mu \mathbf{n}\cdot\partial_\mu \mathbf{n}) - \xi_s \sum_\mu (\mathbf{m}\cdot\partial_\mu \mathbf{n}) + \frac{K_s}{2} n_z^2. \tag{6}$$

where $\rho_s = 2S$ is the magnitude of the staggered spin angular momentum per unit cell, χ_m is the magnetic susceptibility, $A = 2\zeta a^2 JS^2$ is the exchange stiffness, and $\xi_s = 2\zeta aJS^2$ signifies the amplitude of the parity-breaking term. In the absence of a strong external magnetic field, the spin density field $\mathbf{m}$ is a slave variable ($|\mathbf{m}| \ll 1$) that follows the temporal and spatial evolution of the staggered AFM order as[32,33,35]

$$\mathbf{m}/\chi_m = \rho_s(\partial_t \mathbf{n}\times\mathbf{n}) - \xi_s \partial_\mu \mathbf{n}. \tag{7}$$

Eliminating $\mathbf{m}$ we obtain the two-component Klein–Gordon equation for $|\psi_n\rangle = (n_x + in_y, n_x - in_y)^T$ as

$$\left(\partial_z^2 - \frac{1}{c^2}\partial_t^2\right)|\psi_n\rangle = \mathcal{K}_z|\psi_n\rangle, \tag{8}$$

where $c = 2aJ_S/\hbar$ is the spin wave velocity, and $\mathcal{K}_z = K_S(K_S + 4J_S)/(4J_S^2 a^2)$ determines the spin wave gap. Obviously, ψ_n^+ (i.e., $n_x + in_y$) and ψ_n^- (i.e., $n_x - in_y$) are associated with the degenerate left- and right-handed chiral magnons, respectively. Conventional magnons without a spatial phase structure (i.e., without OAM) exhibit opposite intrinsic magnetization of the left- and right-handed modes. Upon time averaging, we find

$$\langle m_L^z\rangle \propto \Im[\psi_n^+ \partial_t (\psi_n^+)^\star] = +\omega_k \rho_n^+, \tag{9}$$

$$\langle m_R^z\rangle \propto \Im[(\psi_n^-)^\star \partial_t \psi_n^-] = -\omega_k \rho_n^-, \tag{10}$$

which clarifies the chiral character of the modes.

Now we show the existence of eigenmodes characterized (in addition to their chirality) by a definite amount of magnonic (meaning akin to the quasiparticles, magnons) OAM. We term these helical modes as twisted AFM magnons.

Twisted AFM magnons

In an extended cylindrical AFM tube and in cylindrical coordinates $\mathbf{r} \to (r, \phi, z)$, the above Klein–Gordon equation admits the non-diffractive Bessel solutions

$$\psi_n(\mathbf{r}, t) \propto J_\ell(k_\perp r)\exp(i\ell\phi + ik_z z)\exp(-i\omega t), \tag{11}$$

with $\ell = 0, \pm1, \pm2, \ldots$. $J_\ell(x)$ is the Bessel function of the first kind with order ℓ. For a cylindrical waveguide which is narrow compared to the magnon wavelength one may apply the paraxial approximation $\mathbf{k}^2 \gg (\mathbf{k}^2 - k_z^2)$, i.e., the transverse wave number $k_\perp$ is small. One finds then that $\partial_z^2 \simeq k^2 + 2ik\partial_z$ leading to the Schrödinger-type equation for the spin waves

$$i\frac{\partial\psi_n}{\partial\tilde{z}} = -\left[\frac{1}{r}\frac{\partial}{\partial r}\left(r\frac{\partial}{\partial r}\right) + \frac{1}{r^2}\frac{\partial^2}{\partial\phi^2} + k^2\right]\psi_n, \tag{12}$$

where $\tilde{z} = z/2k$ can be interpreted as the independent "time-like" variable. We conclude that in the AFM waveguides the modes are transversely confined Laguerre-Gaussian (LG) beams

$$\psi_{\ell,\varsigma}^{LG} \propto \left(\frac{r}{w(z)}\right)^{|\ell|} L_\varsigma^{|\ell|}\left(\frac{2r^2}{w(z)^2}\right) \times \exp\left(-\frac{r^2}{w(z)^2} + ik\frac{r^2}{2R(z)^2}\right) e^{i\ell\phi + ikz} e^{i(2\varsigma + |\ell| + 1)\eta(z)}, \tag{13}$$

where $L_\varsigma^{|\ell|}$ are the generalized Laguerre polynomials, $\ell = 0, \pm1, \pm2, \ldots$; $\varsigma = 0, 1, 2, \ldots$ is the radial quantum number, $w(z) = w_0\sqrt{1 + z^2/z_R^2}$ is the beam width depending on z due to diffraction, $R(z) = z(1 + z_R^2/z^2)$ is the radius of curvature of the wave fronts, and $\eta(z) = \arctan(z/z_R)$. The last exponential factor $(2\varsigma + |\ell| + 1)\eta(z)$ is related to the Gouy phase yielding an additional phase delay on the beam propagation. LG modes have well-defined azimuthal and radial wavefront distributions (quantified by ℓ and ς, respectively) and they form an orthogonal and complete basis in terms of which an arbitrary function can be represented. The existence and utility of twisted modes for various systems ranging from electrons and neutron to acoustic waves are documented[25,38–42]. In AFM the underlying symmetries, free-energy density and the generic equations of motions are different from known cases, yet twisted AFM modes carrying OAM do exist under appropriate setting. To inspect the properties of the canonical OAM, we consider the continuity equation for spin angular momentum transfer in AFMs[35], $\rho_s\partial_t\mathbf{m} + \sum_\mu \partial_\mu \mathcal{J}_\mathbf{m}^\mu = \mathbf{0}$. The spin current along the μ spatial direction reads

$$\mathcal{J}_\mathbf{m}^\mu = -\frac{\rho_s\xi_s}{\chi_m}\partial_t\mathbf{n} - \mathcal{A}(\mathbf{n}\times\partial_\mu\mathbf{n}). \tag{14}$$

The first temporal term on the r. h. s. is determined by the precession of the staggered field $\mathbf{n}$ and thus carries the magnon chirality of any type of magnon beams. The second term is intimately related to the spatial topology of the (helical) magnon wave. In particular, the spatial phase modulations of the spin wave whose twist is characterize by the integer ℓ is decisive. For example, in terms of the left-handed Bessel/LG beams, one finds the conserved z-component of the magnonic spin current

$$\mathcal{J}_{m_z}^\mu = \mathcal{A}\Im[\psi_n^+\partial_\mu(\psi_n^+)^\star] = -\mathcal{A}\rho_\ell^+(r)\left(\frac{\ell}{r}\mathbf{e}_\phi + k_z\mathbf{e}_z\right), \tag{15}$$

where ρ_ℓ^+ is the magnon density of twisted, left-hand chiral magnons. ℓ characterizes the z-component of the intrinsic OAM of the respective mode, $L_z \sim \hbar\ell$ that is independent on the choice of the coordinate origin[25] and different ℓ correspond to different modes, implying that these modes may serve as multiplex information channels. We note that ℓ is unbounded and akin to the geometry and topology of the waveguide, presenting an additional twist that is independent of the magnon chirality. Due to (Gilbert) damping of magnetization procession, the magnon density is a time-decaying function. OAM ℓ however, is robust to damping, meaning when functionalized ℓ for information transmission, the signal becomes weaker with time but the information content is preserved. Further micromagentic

simulations show that ℓ is a global property of the waveguide and is less affected by reasonable variations of deformation in the shape.

DMI coupling, Faraday effects, and electric field control

For controlling twisted AFM magnons with electric means, the electric-field-tunable interfacial DMI can be used to realize twisted spin wave computing. The break of the inversion symmetry at the cylindrical surface along the radial direction $\mathbf{e}_r$ allows for a DMI of the following form, $\mathcal{H}_{\rm DM} = -\mathbf{D}_{ij}\cdot(\mathbf{S}_i\times\mathbf{S}_j)$. The DMI vector reads $\mathbf{D}_{ij} = D(\mathbf{e}_r\times\mathbf{r}_{ij})$. The DMI adds to the Lagrangian density as $\mathcal{L}_{\rm DM} = D_S\big[\mathbf{n}\cdot(\tilde{\nabla}\times\mathbf{n}) + \tilde{\nabla}\cdot(\mathbf{n}\times\mathbf{m}) - \mathbf{m}\cdot(\tilde{\nabla}\times\mathbf{m})\big]$. where $D_S = DS^2$ and $\tilde{\nabla} = (\mathbf{e}_r\times\nabla_{\mathbf{r}_{ij}})$. The second term on the r. h. s. is a parity-breaking term and has the structure of a total derivative. Hence, it does not affect the local dynamics. Dropping the small last higher-order term on the r. h. s. ($\mathbf{m}\ll 1$), we arrive at the in-plane DMI density (note, $\mathbf{r}_{ij}\in xy$-plane)

$$\mathcal{L}^{xy}_{\rm DM} = -D_S/r\left(n_x\partial_\phi n_y - n_y\partial_\phi n_x\right). \tag{16}$$

Otherwise, $\mathbf{r}_{ij}\|\mathbf{e}_z$ results in the longitudinal DMI density

$$\mathcal{L}^{z}_{\rm DM} = -D_S\mathbf{n}\cdot\partial_z[n_z\cos\phi, n_z\sin\phi, -(n_x\cos\phi + n_y\sin\phi)]. \tag{17}$$

Up to the second order in the transversal fluctuations around the equilibrium of $\mathbf{n}$, $\mathcal{L}^z_{\rm DM}$ does not affect the magnon dynamics but pins Walker-type domain walls to the right-Néel type.

The Euler–Lagrange dynamics for the staggered field, Eq. (6) is augmented by an additional term in the presence of DMI. To a leading order in the density $\mathcal{L}^z_{\rm DM}$, the magnon dynamics is governed by

$$\left[\partial_\mu^2 - \frac{1}{c^2}\partial_t^2 + i\sigma_z\mathcal{D}\partial_\phi\right]|\psi_n\rangle = \mathcal{K}_z|\psi_n\rangle, \tag{18}$$

where $\mathcal{D} = \frac{D_S}{AR}$ with R being the radius of the AFM tube. Note, the thickness scaling as r/R of the interface-induced DMI (i.e., $D_S\sim r/R$) has been used to derive Eq. (18). In the absence of DMI ($\mathcal{D}=0$), the topological charge ℓ is independent of the helicity of spin waves and the left-handed ($\psi^+_{\ell,\varsigma}$) and right-handed ($\psi^-_{\ell,\varsigma}$) chiral modes with arbitrary topological charges ℓ are degenerate. This infinite degeneracy is however lifted by the introduction of $\mathcal{L}^{xy}_{\rm DM}$ which behaves as a fictitious electric field that couples to the magnons via the Aharanov–Casher effect. For Bessel/LG modes as solutions for Eq. (18) we infer the modified dispersion relation of the chiral magnons

$$\omega^2_\pm = c^2\left(k_z^2 + k_\perp^2 \pm \mathcal{D}\ell + \mathcal{K}_z\right). \tag{19}$$

The energy dispersion is now dependent on the topological charge ℓ. The spin wave gap is softened by the DMI, meaning that even below the AFM resonance point at $\omega_R = c\sqrt{\mathcal{K}_z}$, twisted magnons can be excited. Equation (19) indicates that the chiral degeneracy of left- and right-handed magnons ($\psi^\pm_{\ell,\varsigma}$) with same topological charge ℓ is lifted, however, the twofold topological $\pm\ell$ degeneracy survives in the presence of interfacial DMI. These degenerate twisted beams with opposite topological charge are decoupled from each other. The OAM-balanced superposition $|\chi_\phi\rangle$ is thus robust to the surface-induced DMI. The Bloch circles and the interference patterns are rotated during propagation along the waveguide resulting in a Faraday effect (cf. Fig. 2)[43–45]. In the paraxial approximation with relatively small transverse kinetic energy, the allowed wave numbers are approximated as $k^z_\pm \simeq k + \delta k^z_\pm$ with $\delta k^z_\pm = \pm\mathcal{D}\ell/(2k) + \mathcal{K}_z/(2k)$. The DMI modifies the longitudinal wave vector resulting in an additional phase difference $\delta\varphi(z)\propto(\mathcal{D}\ell z/k)$. Let l be the length of the AFM tube, then $\delta\varphi(l)=\pi$ can be realized since arbitrarily large values of ℓ are possible allowing so for any desired phase shift even at very weak DMI and the twisted magnon beams exhibit so a rich magneto-electric interference pattern. It is worth noting that such electrical control of the flow of OAM-carrying magnon beams can be directly realized by applying an external electric field through the Aharonov–Casher (AC) effect[25].

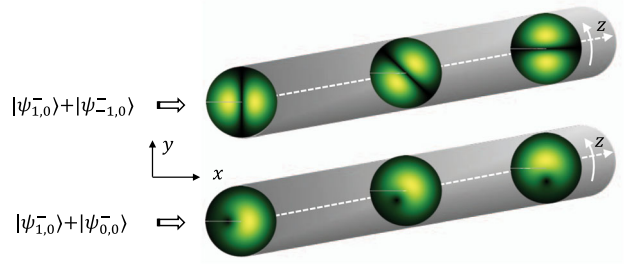

Fig. 2 Faraday effects. Propagation of the interference patterns of the OAM-balanced ($|\psi^-_{1,0}\rangle + |\psi^-_{-1,0}\rangle$) and OAM-unbalanced ($|\psi^-_{1,0}\rangle + |\psi^-_{0,0}\rangle$) superpositions along a AFM waveguide with the interfacial-induced DMI.

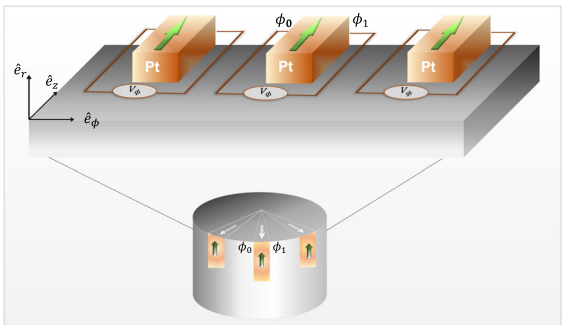

Fig. 3 Angular resolved ISHE measurement. Detections of the pumped spin density $\mathcal{I}^z_s$ of the state $\cos\vartheta_\ell|R\rangle$ by the ϕ-resolved ISHE. At the waveguide end, the z-polarized spins (green arrows) radially pumped into a narrow Pt layers result in an inverse spin Hall voltage $V_\phi\sim\cos^2\vartheta_\ell$ with $\vartheta_\ell\approx\ell(\phi_0+\phi_1)/2$.

OAM-based information coding and AFM logic gates

A conventional way to read/detect the magnonically encoded data is to convert the signal back to electronic signals via the combination of two physical effects: spin pumping and the inverse spin Hall effect (ISHE). In terms of the staggered AFM order parameter $\mathbf{n}$, there are two types of pumping effect generated by the spin current: the pumped spin density ($\mathcal{I}_s\sim\mathbf{n}\times\partial_t\mathbf{n}$) and the staggered spin pumping ($\mathcal{I}_{ss}\sim\partial_\mu[\mathbf{n}\times\partial_t\mathbf{n}]$) representing the imbalance between the spin current carried by the two sublattices[46]. Averaging over time only the $\mathcal{I}^z_s$ and $\mathcal{I}^z_{ss}$ contribute to the DC pumped spin density, in contrast to the x-and y-components of $\mathcal{I}_s$ (and $\mathcal{I}_{ss}$ as well). Integrating further over the cross section we find that $\langle\mathcal{I}^z_s\rangle$ and $\langle\mathcal{I}^z_{ss}\rangle$ do not depend on the internal phase (spatial) structure of the modes (and hence no dependence on ℓ is present). However, a ϕ-resolved analysis evidences a spatial distribution of pumped spin density. For instance, the state $\cos\vartheta_\ell|R\rangle$ (with $\vartheta_\ell=\ell\phi$) gives rise to

$$\mathcal{I}^z_s\propto\omega_k\cos^2\vartheta_\ell \text{ and } \mathcal{I}^z_{ss}\propto-\frac{\ell}{\mathrm{r}}\omega_k\sin 2\vartheta_\ell. \tag{20}$$

These inhomogeneous spin densities can be detected by the ϕ-resolved ISHE, as demonstrated in Fig. 3.

With this we arrive at a key result: The helical or twisted chiral magnons propagating along the same direction in an AFM waveguide are exploitable for realizing parallel logic gates[47]. For a demonstration we recall that $\cos\vartheta_\ell|R\rangle$, $\sin\vartheta_\ell|R\rangle$, $\cos\vartheta_\ell|L\rangle$, and

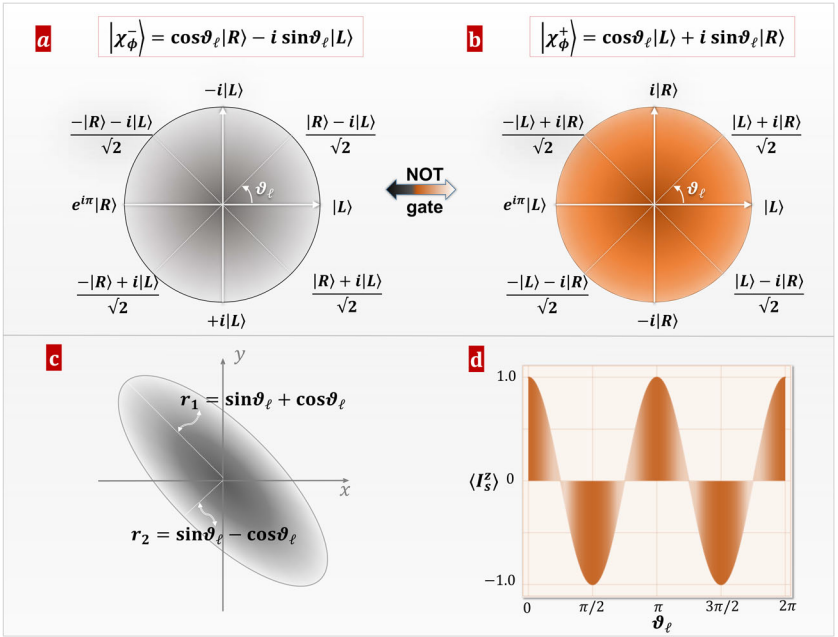

Fig. 4 OAM-based AFM logic gates. a and **b** Logic gates realized by the OAM-balanced twisted AFM chiral magnon states with opposite topological charge ℓ. **c** Corresponding elliptical precession orbit of the chiral magnon state $|\chi_\phi^-\rangle$ in the *x*–*y* plane. **d** Pumped spin accumulation for which the DC component is given by the area of the ellipse: $\langle \mathcal{I}_s^z\rangle = \langle \partial_t \mathbf{n}\times\mathbf{n}\rangle \sim \cos 2\vartheta_\ell$.

$\sin\vartheta_\ell|L\rangle$ are four-fold degenerate states. Our logic gates are realized then as follows:

(i) **Phase shift** (R_ϕ) **gates** with OAM-unbalanced superposition of two chiral magnon beams with topological charge 0 and ℓ,

$$|\chi_\phi\rangle = |R\rangle + e^{i\vartheta_\ell}|L\rangle. \tag{21}$$

Some special examples are: *T-gate* with $\vartheta_\ell = \pi/4$, *S-gate* with $\vartheta_\ell = \pi/2$, and the *phase-flip Pauli-Z gate* with $\vartheta_\ell = \pi$.

(ii) **Hadamard (H) gate** with OAM-balanced superposition of two chiral magnon eigenmodes with opposite topological charges $\pm\ell$, meaning

$$\begin{aligned}|\chi_\phi\rangle &= e^{i\vartheta_\ell}|R\rangle + e^{-i\vartheta_\ell}|L\rangle \\ &= \cos\vartheta_\ell(|R\rangle + |L\rangle) + i\sin\vartheta_\ell(|R\rangle - |L\rangle).\end{aligned} \tag{22}$$

We may rewrite the above superposition into two Bloch circles as, $|\chi_\phi\rangle = |\chi_\phi^+\rangle + |\chi_\phi^-\rangle$ with

$$|\chi_\phi^-\rangle = \cos\vartheta_\ell|R\rangle - i\sin\vartheta_\ell|L\rangle, \tag{23}$$

$$|\chi_\phi^+\rangle = \cos\vartheta_\ell|L\rangle + i\sin\vartheta_\ell||R\rangle. \tag{24}$$

We have then the *NOT (Pauli-X)* connecting $|\chi_\phi^\pm\rangle$, the *Pauli-Y gates* with $|R\rangle \to i|L\rangle$ and $|L\rangle \to -i|R\rangle$, and *the square root of NOT gates* with $|R\rangle \to [(1+i)|R\rangle + (1-i)|L\rangle]/2$ and $|L\rangle \to [(1-i)|R\rangle + (1+i)|L\rangle]/2$, as demonstrated in Fig. 4a, b.

Without breaking the time-reversal $\mathcal{T}$ and/or sublattice exchange $\mathcal{I}$ symmetries, the parallel manipulations of magnon chiralities are thus fully realized in the AFM waveguides with an additional degree of freedom, the topological charge ℓ. Such particular chiral magnon state $|\chi_\phi\rangle$ can be electrically read out by virtue of spin pumping[46] (cf. Figs. 3 and 4 c/d).

Simulations for experimental realization

The preceding derivations are fully general. To confirm the robustness of the predictions when accounting for material and geometry specific effects that are important for an experimental realization, it is instructive to perform full-fledged numerical simulations for a specific waveguide. To this end, let us consider the G-type AFM waveguide made of NiO with material parameters determined by the previous experimental and theoretical studies. For conducting micromagnetic simulations we discretized the waveguide into boxes with a size of the atomic lattice constant of 0.418 nm[348]. Based on previous investigations and our own initial calculations for a cylindrical model system, we estimate the relevant frequency regime to be around $f \sim 0.5$ THz. In the following we use a 0.5 THz frequency for the exciting field and investigate different setups with a special focus on the impact of different topological charges and helicities of the spin waves. Details on the spin dynamics simulations including the spatial and temporal profile of the applied field can be found in the Supplementary Methods.

Twisted wave packet propagation

To demonstrate the twisted wave packets propagation, we consider a waveguide with 100 × 100 × 300 unit cells (u. c.) excited at one end by a twisted magnetic field. For the frequency of 0.5 THz, the wavelength of the plane-wave mode is $\lambda \approx 30.5$ nm. The boundaries are modeled such that they absorb most of the incoming magnons by introducing an exponentially increasing damping parameter in a tube shell with a 20 u. c. thickness. This helps avoiding reflection effects in order to focus on the core features of twisted magnon beams. Because of the discrete rotational symmetry characterized by the OAM, twisted magnon modes are protected against perturbations including defects and finite size effects as discussed for the case of a FM wave guide in ref. [49]. An example of a few-cycle wave packet propagating along the NiO wire is shown in Fig. 5a.

For further insight, let us continue with different wave packets propagating along the wire, especially focusing on the group velocity, broadening, and signal decay.

In Fig. 5b, few-cycle twisted AFM pulses are propagated along the wire, and the position of maximum magnon density is tracked. For this calculation, only one line of magnetic moments parallel to the *z*-axis is analyzed. The offset to the center is 25 u. c. (≈10 nm).

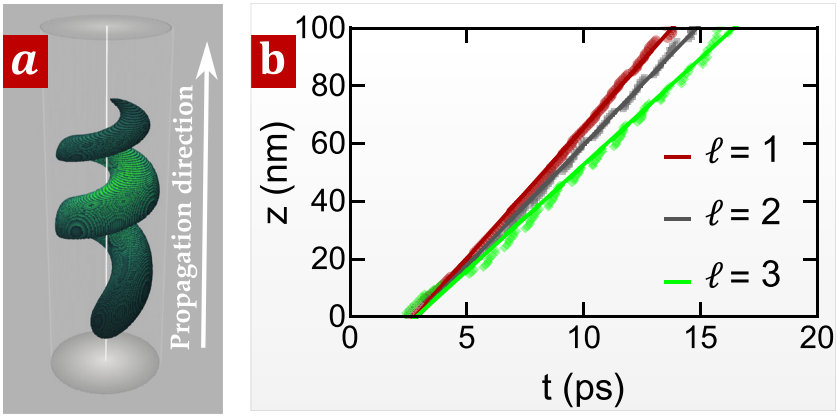

Fig. 5 Propagation of a twisted magnon wave pulse in an AFM waveguide. a A snapshot of the twisted AFM magnonic pulse with $\ell = 1$ taken 10 ps after being triggered with the magnetic field of a THz pulse focused on one end of the waveguide. n_x component of the staggered field is shown. **b** Speed comparison for few-cycle twisted magnonic wave packets carrying different OAM.

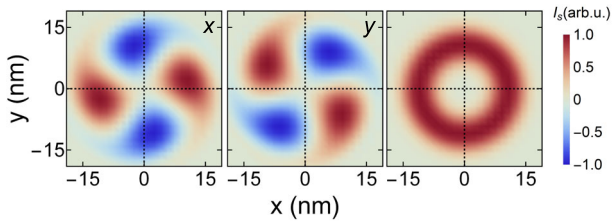

Fig. 6 Cross section of the ISHE signal. The spin accumulation due to a twisted magnon wave packet with $\ell = 2$ and left-handed (clockwise) chirality is calculated according to the ISHE via $\mathcal{I}_s \sim \mathbf{n} \times \partial_t \mathbf{n}$. The three panels display the different components of the induced spin-current showing that only the *z*-component delivers a non-zero value after integration over the whole cross section. The staggered magnetization is obtained from full-numerical spin dynamics simulations.

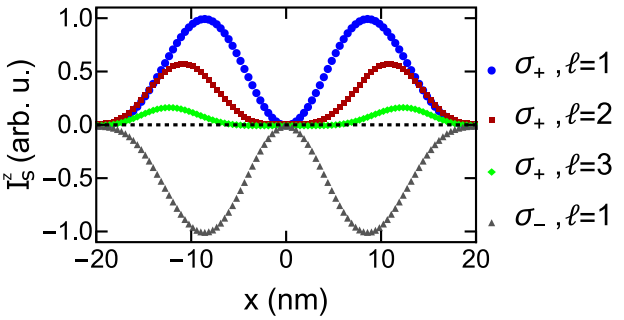

Fig. 7 Spatial profile of the time-integrated out-of-plane ISHE signal. Twisted magnon waves for different topological charges and chiralities are generated in the NiO waveguide. The resulting *z*-component of the spin accumulation according to the ISHE is calculated via $\mathcal{I}_s \sim \mathbf{n} \times \partial_t \mathbf{n}$.

The group velocities are different for different winding numbers ℓ. The linear regressions give velocities of $v_{\ell=1} = 9.09\,\mathrm{km\,s^{-1}}$, $v_{\ell=2} = 8.36\,\mathrm{km\,s^{-1}}$ and $v_{\ell=3} = 7.35\,\mathrm{km\,s^{-1}}$. Also, the signal amplitude decays more rapidly when increasing the topological number.

Spin dynamics induced by twisted AFM beams

In addition to the propagation of AFM twisted magnon beams, the induced electronic spin density at the surface of the tube can be calculated from the spin dynamics calculations. This we do by calculating the staggered magnetization from the full G-type AFM lattice and subsequently calculate the ISHE via $\mathcal{I}_s \sim \mathbf{n} \times \partial_t \mathbf{n}$ for a cross section of the NiO wire. The resulting patterns of the three Cartesian components of pumped spin density $\mathcal{I}_s$ for a beam with $\ell = 2$ are shown in Fig. 6. All signals are normalized with respect to the maximum value for each component. As predicted, only the *z*-component has a completely positive signal, delivering a finite signal when integrating over time. In contrast to that, the *x*- and *y*-components possess a twofold distribution with alternating positive and negative areas eventually summing up to a total induced spin density of zero.

The characteristic features of the *z*-component for different chiralities and topological charges are presented in Fig. 7 for a transversal profile through the center of the wire. Generally, the maximum pumped spin density can be found in the region where the highest magnon amplitudes are expected. This also means that for higher topological charges ℓ, the maximum intensity distance increases (cf. dark red and bright green markers). The diminished intensity is explainable by the higher damping of the magnon amplitudes, which is proportional to the magnon density.

In addition, the sign of the pumped spin density is determined by the chirality of the magnon polarization, meaning that a change from left-handed to right-handed magnons exclusively changes the sign of the signal and not its distribution. Thus, the pumped spin current due to the ISHE delivers a fingerprint for different twisted magnon modes determined by both the chirality and the topological charge of the spin wave. Current efforts are focused on utilizing the twisted beam for driving AFM structures[50–52] where we expect the topology of these beams to add an additional twist on existing AFM magnonics.

Superposed beams—proof of gate operations

In principle, the spin current density profiles shown in Figs. 6 and 7, generated by different types of magnon modes indicate the possibility of an OAM specific detection of signals. In order to close the gap between these results and the concept of parallel information transport and logic gate operations, we now proceed with numerical simulations of superpositions of different magnon modes. We perform spin dynamics calculations as before, but the cylindrical system is now excited with superimposed magnetic fields, each exciting an individual twisted magnon mode.

As an example, the superposition of beams with $\ell = \pm 1$ and positive helicity are excited in the same NiO cylinder as before. The time resolved pumped spin density is shown in Fig. 8 with the reference signal for a single $\ell = 1$ magnon in Fig. 8a. All results have in common, that the excited beams need a finite time to reach the measurement slice at 150 u.c. distance, therefore

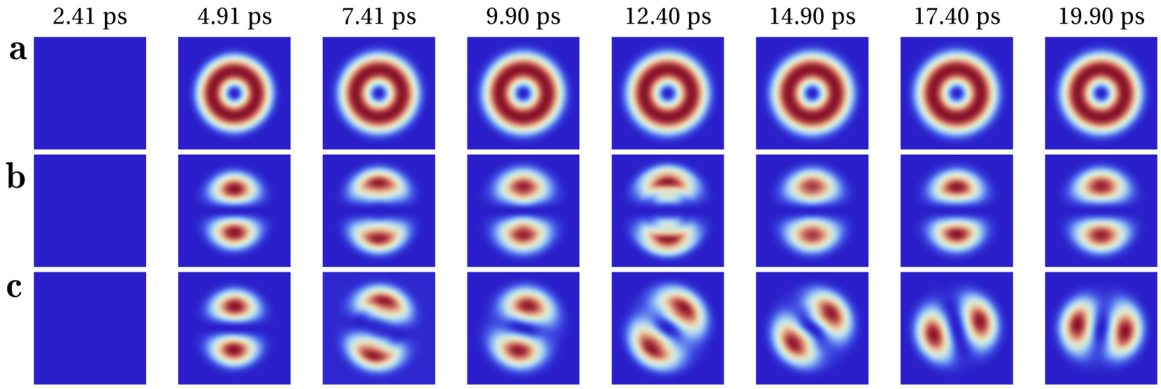

Fig. 8 Time evolution of the out-of-plane ISHE signal. Twisted magnon waves with different compositions are generated in the NiO waveguide. **a** Shows the reference signal, which is the *z*-component of the spin accumulation according to the ISHE is calculated via $\mathcal{I}_s \sim \mathbf{n} \times \partial_t \mathbf{n}$. **b** Shows the superposition of two twisted modes of opposite topological charge $\ell = \pm 1$ and (**c**) the same combination of beams but for a small difference in the frequencies: $f_1 = 0.5$ THz, $f_2 = 1.1 f_1$. The resulting pattern rotates with the beating frequency.

showing no spin accumulation at the first snapshot after 2.41ps. Next, let's consider two monochromatic beams (b, $f_1 = f_2 = 0.5$ THz) and slightly detuned beams (c, $f_1 = f_2/1.1 = 0.5$ THz). Because of the fixed phase difference in case of the monochromatic beam composition, a steady pattern in the ISHE signal is present in Fig. 8b, showing the areas of constructive and destructive interference of the spin waves in contrast to the radially symmetric result in Fig. 8a. The 10% detuned beams exhibit a time dependent phase relation, hence the whole interference pattern rotates over time with a frequency significantly lower than the excitation frequency. Ideally, the beating frequency is $f_B = 0.5|f_2 - f_1| = 0.05 f_1 = 25$ GHz. Therefore, it can be utilized to overcome limitations in the time resolution of the ISHE measurement.

METHODS

Spin dynamics simulations

The predictions are generic. For a material-specific demonstration we used NiO with a material parameters as determined experimentally. For the numerical realizations to assess the analytical predictions and provide experimental guidance, we used the open-source, GPU-accelerated software package `mumax3`[53] for the micromagnetic simulations. Input data and more detailes are provided in the Supplementary Methods.

DATA AVAILABILITY

All data needed to reach the conclusions in the paper are present in the paper and/or the Supplementary Methods and may be requested from the authors.

CODE AVAILABILITY

The codes developed in this study are available from the authors upon reasonable request. The open-source software package `mumax3` is freely available.

Received: 15 March 2021; Accepted: 4 June 2021;
Published online: 05 July 2021

REFERENCES

1. Chumak, A. V., Vasyuchka, V. I., Serga, A. A. & Hillebrands, B. Magnon spintronics. *Nat. Phys.* **11**, 453–461 (2015).
2. Wang, Q. et al. A magnonic directional coupler for integrated magnonic half-adders. *Nat. Electron* **3**, 765–774 (2020).
3. Dieny, B. et al. Opportunities and challenges for spintronics in the microelectronics industry. *Nat. Electron* **3**, 446–459 (2020).
4. Kampfrath, T. Coherent Terahertz Control of Antiferromagnetic Spin Waves. *Nat. Photonics* **5**, 31–34 (2011).
5. Jungwirth, T., Martí, X., Wadley, P. & Wunderlich, J. Antiferromagnetic spintronics. *Nat. Nanotechnol.* **11**, 231–241 (2016).
6. Gomonay, O., Baltz, V., Brataas, A. & Tserkovnyak, Y. Antiferromagnetic spin textures and dynamics. *Nat. Phys.* **14**, 213–216 (2018).
7. Gomonay, E. V. & Loktev, V. M. Spintronics of antiferromagnetic systems (Review Article). *Low. Temp. Phys.* **40**, 17–35 (2014).
8. Šmejkal, L., Mokrousov, Y., Yan, B. & MacDonald, A. H. Topological antiferromagnetic spintronics. *Nat. Phys.* **14**, 242–251 (2018).
9. Jungwirth, T. et al. The multiple directions of antiferromagnetic spintronics. *Nat. Phys.* **14**, 200–203 (2018).
10. Baltz, V. Antiferromagnetic spintronics. *Rev. Mod. Phys.* **90**, 015005 (2018).
11. Fukami, S., Lorenz, V. O. & Gomonay, O. Antiferromagnetic spintronics. *J. Appl. Phys.* **128**, 070401 (2020).
12. Duine, R. A., Lee, K.-J., Parkin, S. S. P. & Stiles, M. D. Synthetic antiferromagnetic spintronics. *Nat. Phys.* **14**, 217 (2018).
13. Lavrijsen, R. et al. Magnetic ratchet for three-dimensional spintronic memory and logic. *Nature* **493**, 647 (2013).
14. Yang, S.-H., Ryu, K.-S. & Parkin, S. S. P. Domain-wall velocities of up to 750 m s^{-1} driven by exchange-coupling torque in synthetic antiferromagnets. *Nat. Nanotechnol.* **10**, 221 (2015).
15. Huang, B. Layer-dependent ferromagnetism in a van der Waals crystal down to the monolayer limit. *Nature* **546**, 270 (2017).
16. Gong, C. Discovery of intrinsic ferromagnetism in two-dimensional van der Waals crystals. *Nature* **546**, 265 (2017).
17. Xing, W. Electric field effect in multilayer $Cr_2Ge_2Te_6$: a ferromagnetic 2D material. *2D Mater.* **4**, 024009 (2017).
18. Wang, X. Raman spectroscopy of atomically thin two-dimensional magnetic iron phosphorus trisulfide ($FePS_3$) crystals. *2D Mater.* **3**, 031009 (2016).
19. Lee, J.-U. Ising-Type Magnetic Ordering in Atomically Thin $FePS_3$. *Nano Lett.* **16**, 7433 (2016).
20. Xing, W. Magnon Transport in Quasi-Two-Dimensional van der Waals Antiferromagnets. *Phys. Rev. X* **9**, 011026 (2019).
21. Kittel, C. Theory of Antiferromagnetic Resonance. *Phys. Rev.* **82**, 565 (1951).
22. Keffer, F. & Kittel, C. Theory of Antiferromagnetic Resonance. *Phys. Rev.* **85**, 329 (1952).
23. Willner, A. E. Optical communications using orbital angular momentum beams. *Adv. Opt. Photon.* **7**, 66 (2015).
24. Bozinovic, N. Terabit-Scale Orbital Angular Momentum Mode Division Multiplexing in Fibers. *Science* **340**, 1545 (2013).
25. Jia, C. L., Ma, D. C., Schäffer, A. F. & Berakdar, J. Twisted magnon beams carrying orbital angular momentum. *Nat. Commun.* **10**, 2077 (2019).
26. Chen, M., Schäffer, A. F., Berakdar, J. & Jia, C. L. Generation, electric detection, and orbital-angular momentum tunneling of twisted magnons. *Appl. Phys. Lett.* **116**, 172403 (2020).
27. Dzyaloshinsky, I. A thermodynamic theory of "weak" ferromagnetism of antiferromagnetics. *J. Phys. Chem. Solids* **4**, 241 (1958).
28. Moriya, T. Anisotropic Superexchange Interaction and Weak Ferromagnetism. *Phys. Rev.* **120**, 91 (1960).
29. Liu, Y., Sellmyer, D. J. & Shindo, D. *Handbook of Advanced Magnetic Materials* (Springer, 2006).
30. Auerbach, A. *Interacting Electrons and Quantum Magnetism* (Springer-Verlag, Inc. 1994).

31. Nakata, K., Kim, S. K., Klinovaja, J. & Loss, D. Magnonic topological insulators in antiferromagnets. *Phys. Rev. B* **96**, 224414 (2017).
32. Haldane, F. D. M. Nonlinear Field Theory of Large-Spin Heisenberg Antiferromagnets: semiclassically Quantized Solitons of the One-Dimensional Easy-Axis Néel State. *Phys. Rev. Lett.* **50**, 1153–1156 (1983).
33. Ivanov, B. A. & Kolezhuk, A. K. Solitons with Internal Degrees of Freedom in 1D Heisenberg Antiferromagnets. *Phys. Rev. Lett.* **74**, 1859 (1995).
34. Ivanov, B. A. Spin dynamics of antiferromagnets under action of femtosecond laser pulses (Review Article). *Low. Temp. Phys.* **40**, 91–105 (2014).
35. Tveten, E. G., Müller, T., Linder, J. & Brataas, A. Intrinsic magnetization of antiferromagnetic textures. *Phys. Rev. B* **93**, 104408 (2016).
36. Delfino, F., Pelissetto, A. & Vicari, E. Three-dimensional antiferromagnetic CPN-1 models. *Phys. Rev. E* **91**, 052109 (2015).
37. Cheng, R., Okamoto, S. & Xiao, D. Spin Nernst Effect of Magnons in Collinear Antiferromagnets. *Phys. Rev. Lett.* **117**, 217202 (2016).
38. Allen, L., Beijersbergen, M. W., Spreeuw, R. J. C. & Woerdman, J. P. Orbital angular momentum of light and the transformation of Laguerre-Gaussian laser modes. *Phys. Rev. A* **45**, 8185 (1992).
39. Yao, A. M. & Padgett, M. J. Orbital angular momentum: origins, behavior and applications. *Adv. Opt. Photon.* **3**, 161 (2011).
40. Uchida, M. & Tonomura, A. Generation of electron beams carrying orbital angular momentum. *Nature* **464**, 737 (2010).
41. Verbeeck, J., Tian, H. & Schattschneider, P. Production and application of electron vortex beams. *Nature* **467**, 301 (2010).
42. Clark, C. W. Controlling Neutron Orbital Angular Momentum. *Nature* **525**, 504 (2015).
43. Greenshields, C., Stamps, R. L. & Franke-Arnold, S. Vacuum Faraday effect for electrons. *N. J. Phys.* **14**, 103040 (2012).
44. Tveten, E. G., Qaiumzadeh, A. & Brataas, A. Antiferromagnetic Domain Wall Motion Induced by Spin Waves. *Phys. Rev. Lett.* **112**, 147204 (2014).
45. Tadic, M., Nikolic, D., Panjan, M. & Blake, G. R. Magnetic properties of NiO (nickel oxide) nanoparticles: blocking temperature and Neel temperature. *J. All. Comp.* **647**, 1061 - 1068 (2015).
46. Cheng, R., Xiao, J., Niu, Q. & Brataas, A. Spin Pumping and Spin-Transfer Torques in Antiferromagnets. *Phys. Rev. Lett.* **113**, 057601 (2014).
47. Nielsen, M. A. & Chuang I. L. *Quantum Computation and Quantum Information* (Cambridge University Press, 2010).
48. Coey, J. M. D. *Magnetism and magnetic materials* (Cambridge University Press, 2010).
49. Jia, C., Ma, D., Schäffer, A. F. & Berakdar, J. Twisting and tweezing the spin wave: on vortices, skyrmions, helical waves, and the magnonic spiral phase plate. *J. Opt.* **21**, 124001 (2019).
50. Cheng, R., Daniels, M. W., Zhu, J.-G. & Xiao, D. Antiferromagnetic Spin Wave Field-Effect Transistor. *Sci. Rep.* **6**, 24223 (2016).
51. Lan, J., Yu, W. & Xiao, J. Antiferromagnetic domain wall as spin wave polarizer and retarder. *Nat. Commun.* **8**, 178 (2017).
52. Qaiumzadeh, A., Kristiansen, L. A. & Brataas, A. Controlling chiral domain walls in antiferromagnets using spin-wave helicity. *Phys. Rev. B* **97**, 020402(R) (2018).
53. Vansteenkiste, A. et al. The design and verification of MuMax3. *AIP Adv.* **4**, 107133 (2014).

ACKNOWLEDGEMENTS

This work is supported by the National Natural Science Foundation of China (No. 91963201, and 11834005), the German Research Foundation (SFB TRR 227), and the 111 Project under Grant No. B2006.

AUTHOR CONTRIBUTIONS

All authors contributed to the performance of the project and to the discussion and the writing of the paper.

FUNDING

Open Access funding enabled and organized by Projekt DEAL.

COMPETING INTERESTS

The authors declare no competing interests.

ADDITIONAL INFORMATION

Supplementary information The online version contains supplementary material available at https://doi.org/10.1038/s41524-021-00570-0.

Correspondence and requests for materials should be addressed to C.J. or J.B.

Reprints and permission information is available at http://www.nature.com/reprints

Publisher's note Springer Nature remains neutral with regard to jurisdictional claims in published maps and institutional affiliations.